



Effect of substrate preheating on the texture, phase and nanohardness of a Ti–45Al–2Cr–5Nb alloy processed by selective laser melting

Wei Li, Jie Liu, Yan Zhou, Shifeng Wen, Qingsong Wei *, Chunze Yan *, Yusheng Shi

State Key Laboratory of Materials Processing and Die & Mould Technology, School of Materials Science and Engineering, Huazhong University of Science and Technology, Wuhan 430074, China

ARTICLE INFO

Article history:

Received 10 January 2016

Received in revised form 16 February 2016

Accepted 17 February 2016

Available online 14 March 2016

Keywords:

Selective laser melting

Ti–45Al–2Cr–5Nb alloy

Texture

Phase

Nanohardness

ABSTRACT

The crystallographic texture, phase composition and evolution, and nanohardness of a Ti–45Al–2Cr–5Nb alloy processed by selective laser melting (SLM) at various substrate preheating temperatures were investigated. The α_2 phase decreases whereas the γ and B_2 phases increase with increasing preheating temperature, and the relationship in orientation between B_2 , α_2 and γ phases is described as follows: $(11\bar{2}0)\alpha_2 // (111)\gamma // (111)B_2$. The SLM-processed TiAl alloy shows much higher nanohardness than its traditional casting counterpart, which increases with the increase of preheating temperature. The findings would be a valuable reference for fabricating TiAl components with acceptable texture, phase compositions and nanohardness by SLM.

© 2016 Elsevier Ltd. All rights reserved.

TiAl-based alloys are considered as extremely promising candidates for aerospace and aircraft applications due to their extremely high specific stiffness, hardness and yield strength and excellent creep resistance at elevated temperature [1–5]. Their inherent low room temperature ductility and poor hot deformability, however, greatly hinder the production of TiAl-based alloy components for the practical applications [6]. Recently, some special manufacturing techniques such as isothermal forging and hot extrusion have been developed to process TiAl-based alloys and improve the ductility by means of microstructure refinement and phase transformation [7]. However, these thermo-mechanically fabricated components show extremely high costs, heterogeneous microstructure and limited structural complexity [6].

Selective laser melting (SLM) is capable of fabricating near-fully dense and complex metal parts directly from computer-aided design (CAD) models [8–10], therefore showing great potential for fabricating TiAl alloy components with acceptable quality and costs and complex geometries. Recently, some preliminary investigations have been carried out to find the optimal SLM process window for TiAl alloys. Loeber et al. found the existence of cracks and pores in the TiAl samples mainly because the SLM processing parameters were not properly optimized [12]. Löber et al. adopted single track experiments to optimize the SLM processing parameters for a TiAl alloy, and near-fully dense TiAl parts could be achieved [13]. Gussone et al. investigated the effect of SLM processing parameters on the chemical composition and tensile strength of TiAl alloys [14]. However, to the best of the authors' knowledge, few

previous research works studied the grain orientation, crystallographic texture and phase composition of TiAl alloys processed by SLM, and their effects on the mechanical properties of SLM parts. It has been demonstrated that the substrate preheating in the SLM process has an important role in controlling the microstructures and texture of SLM-processed metals [14]. Therefore, this work concentrates on investigating the influence of substrate preheating temperature on the crystallographic texture, phase transition and evolution, and mechanical properties (nanohardness) of a TiAl alloy, Ti–45Al–2Cr–5Nb, processed by SLM.

A Ti–45Al–2Cr–5Nb (at.%) alloy powder with an average particle size (D_{v50}) of 27.6 μm was supplied by Beijing Institute of Aeronautical Materials (BIAM, China). Prior to SLM, the TiAl powder was dried in air at 50 °C for 24 h and sieved (200 mesh) to reduce the aggregated particles and thus improve its flowability. An HRPM-II type SLM machine with a 400 W single-mode ytterbium fiber laser (SP-400C, SPI Lasers, America) was used, and the wavelength and laser beam diameter ($\Phi_{90\%}$) of the laser source were 1069 ± 10 nm and 100 μm , respectively. The SLM process was conducted in a high purity argon atmosphere (99.9%) to avoid the pick-up of reactive oxygen. Based on a series of preliminary experiments, the SLM parameters were optimized as follows: the laser power (P) = 200 W, laser scan speed (V) = 400 mm/s, scan line hatch spacing (h) = 100 μm , and powder layer thickness (d) = 30 μm . Four different levels of substrate preheating temperature, namely 298 K (room temperature), 423 K, 523 K and 623 K were selected in the SLM experiments and the corresponding obtained SLM samples were denoted by T_0 , T_1 , T_2 and T_3 , respectively.

X-ray diffraction (XRD) measurements were performed on a XRD-7000S instrument (Shimadzu, Japan) with a Cu tube at 40 kV and 30 mA. The scattering angular (2θ) varied from 20° to 110° with a

* Corresponding authors at: No.1037 Luoyu Road, Hongshan District, Hubei, Wuhan, China.

E-mail addresses: wqs_xn@163.com (Q. Wei), c_yan@hust.edu.cn (C. Yan).

scan rate of $10^\circ/\text{min}$. The specimens for electron backscattered diffraction (EBSD) examinations were electrolytically polished on LectroPol-5 (Struers, Denmark) at 25 V for 20 s. EBSD was performed on the HKL Nordlys orientation imaging microscope system (Oxford, Oxford Instruments, UK) mounted on a JSM-7600F (JEOL, Japan) scanning electron microscope. Transmission electron microscope (TEM) and high resolution transmission electron microscope (HRTEM) measurements were executed on a JEOL-2100 type machine (JEOL, Japan). Nanoindentation tests were performed using a high-precision nanohardness scratch tester (TI750, Hysitron, American) with the test force of 3500 mN and hold time of 2 s.

Fig. 1(a) illustrates the scanning strategy of the SLM process. The arrows indicate the movement of the laser and 90° rotation angle of the scanning direction between two consecutive layers N and $N + 1$. The inverse pole figure (IPF) is shown in Fig. 1(b), representing the relationship between colors in the EBSD images and crystal orientations of the SLM-processed samples. The EBSD orientation image map and grain boundary misorientation angles of the samples T_0 , T_1 , T_2 and T_3 from the top view are illustrated in Fig. 1(c), (d), (e) and (f), respectively. The applied substrate preheating significantly influences the grain size and orientation of the SLM-processed Ti–45Al–2Cr–5Nb alloy. As the SLM process was carried out at room temperature (298 K) without substrate preheating, the average grain size of T_0 was calculated to be $8.3\text{ }\mu\text{m}$, and the majority of the grains have a green-blue color as shown in Fig. 1(c). The grains at $(10\bar{1}1)$ and $(11\bar{2}1)$ orientations are

present along the laser scanning direction [11]. When the SLM process was conducted at a relatively low substrate preheating temperature of 423 K, the grains generally grew up with an average grain size of $10.2\text{ }\mu\text{m}$. Also, it can be easily found that the red areas increase while the green regions decrease in the EBSD map in Fig. 1(d) compared with that in Fig. 1(c), indicating that the (0001) orientation is strengthened whereas the $(10\bar{1}1)$ orientation is weakened on the top view of sample T_1 . When increasing preheating temperature to 523 K, the grains size further increases and the average size reaches $12.8\text{ }\mu\text{m}$. Moreover, the EBSD orientation map is dominated by reddish color and the green-blue regions are further reduced, as shown in Fig. 1(e). This illustrates that the grains of T_2 reveal a strong (0001) orientation. At an even higher preheating temperature of 623 K, the average grain size attains the maximum of $15.2\text{ }\mu\text{m}$. But, the EBSD map in Fig. 1(f) shows decreased reddish areas but increased green-blue regions compared with that in Fig. 1(e). It is worthy noted that the areas of the three colors basically remain the same with each other, showing that the grains at (0001) , $(10\bar{1}1)$ and $(11\bar{2}1)$ orientations are equally existing in T_3 . The fineness of the grains is determined by thermal gradient (G), the solidification rate (R) and cooling rate ($T = G \times R$) [15]. The higher the cooling rate of the material, the finer the microstructure. The SLM process is able to generate an extremely high cooling rates (10^6 K/s), therefore resulting in a very fine microstructure of the SLM-processed Ti–45Al–2Cr–5Nb. But, the substrate preheating has a negative effect on the cooling rate. With increasing preheating

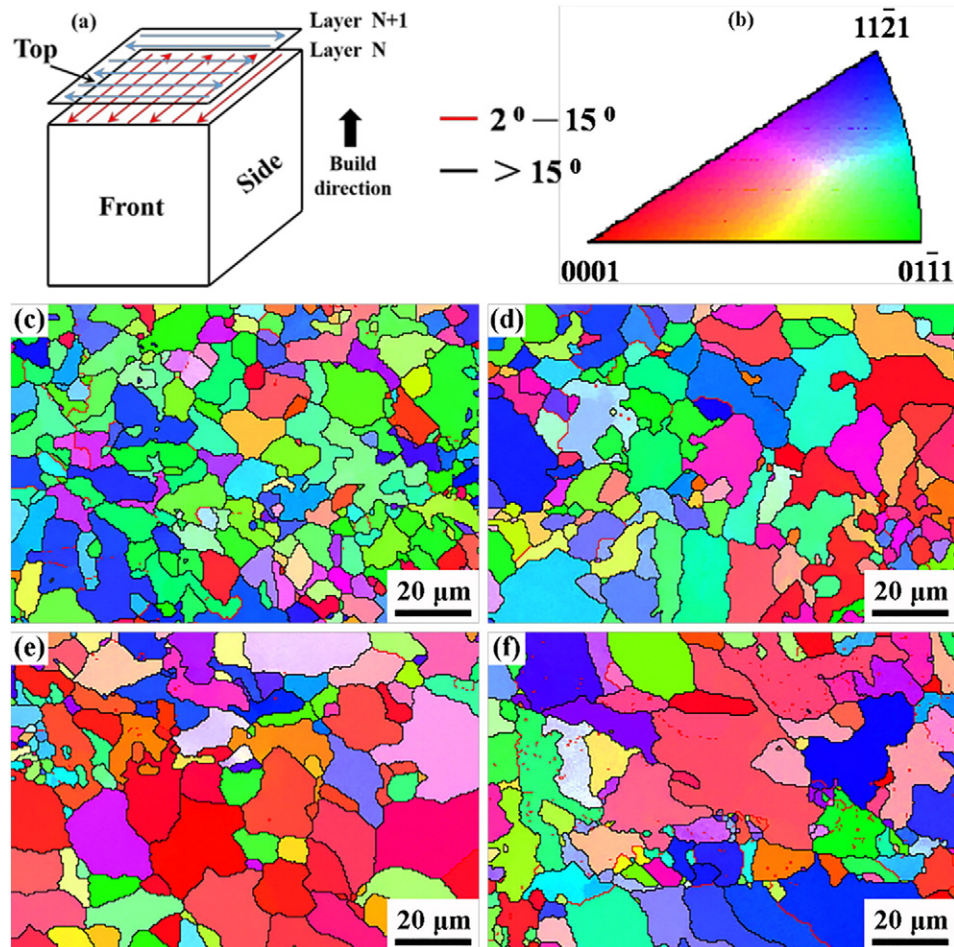


Fig. 1. Scanning strategy of the SLM process (a), the crystal orientation-color relation map referred to as the inverse pole figure (IPF) (b). EBSD orientation maps obtained from the top view of the SLM-processed Ti–45Al–2Cr–5Nb samples of T_0 , T_1 , T_2 and T_3 , which are represented in (c), (d), (e) and (f), respectively.

temperature, the cooling rate decreases, thus leading to growth of the grain size. Consequently, varying substrate preheating temperature can tailor the grains size and orientation of the SLM-processed Ti–45Al–2Cr–5Nb alloy.

The grain boundary misorientation angles of T_0 , T_1 , T_2 and T_3 were also determined through EBSD analysis and divided by low-angle grain boundaries (LAGBs, 2° – 15°) and high-angle grain boundaries (HAGBs, $>15^\circ$). Obviously, the samples T_0 , T_1 , T_2 and T_3 are dominated by HAGBs with the contents of 88.2%, 91.7%, 92.8% and 93.9%, respectively. It is well known that SLM creates parts by layer-wise addition of materials. Due to the high energy of laser beam, when a new layer is created, the previous layer(s) will be partially or completely remelted. This phenomenon leads to recrystallization and then the HAGBs will be aroused. In addition, the content of HAGBs increases with increasing substrate preheating temperature. This is mainly attributed to the fact that the higher preheating temperature brings about a relatively longer duration time in the remelting state and thus prolongs the recrystallization time.

As shown in Fig. 1, there are big differences in the grain orientations between the SLM samples at the different preheating temperatures. Therefore, substrate preheating has a significant influence on the local crystallographic texture of the SLM-processed Ti–45Al–2Cr–5Nb. The most common $\{0001\}$ pole figures (PF) from the top view for the SLM-processed Ti–45Al–2Cr–5Nb samples, T_0 , T_1 , T_2 and T_3 , are represented in Fig. 2(a), (b), (c) and (d), respectively. In the sample fabricated without substrate preheating (T_0), a weaker $\{0001\}$ texture along the scanning direction occurs, as shown in the PF of Fig. 2(a). The low intensities in the PF suggest the presence of a fiber texture [11]. The fiber texture intensity can be described by the texture index, which is

calculated from the orientation distribution function (ODF) $f(g)$ using Eq. (1):

$$\text{Texture Index} = TI = \int_{\text{eulerspace}} (f(g))^2 dg \quad (1)$$

where f is the orientation distribution as a function of the Eulerspace coordinates g . The texture index of sample T_0 was calculated to be 12.54. For isotropic materials, the texture index equals to unity [16]. The texture indexes of T_1 , T_2 and T_3 were determined to be 12.96, 20.00 and 13.68, respectively. The texture index results of T_0 , T_1 , T_2 and T_3 are in a good agreement with the EBSD orientation maps shown in Fig. 1(c)–(f). In order to further investigate the effect of substrate preheating on the texture evolution, the normalized texture difference is introduced. The normalized texture difference between samples T_0 and T_x with respect to sample T_0 can be calculated by Eq. (2):

$$\begin{aligned} \text{Normalized Texture Difference} &= NTD \\ &= \frac{\int_{\text{eulerspace}} (f_{T_0}(g) - f_{T_x}(g))^2 dg}{\int_{\text{eulerspace}} (f_{T_0}(g))^2 dg} \end{aligned} \quad (2)$$

where $f_{T_0}(g)$ and $f_{T_x}(g)$ were the ODF of samples T_0 and T_x ($x = 1, 2, 3$) respectively, as a function of the Euler space coordinates g . The normalized texture differences of T_1 , T_2 and T_3 with respect to T_0 were calculated to be 0.11%, 35.39% and 0.83%, respectively. Therefore, it is evident that the substrate preheating temperatures at 423 K and 623 K have little effect on the crystallographic texture while the substrate preheating

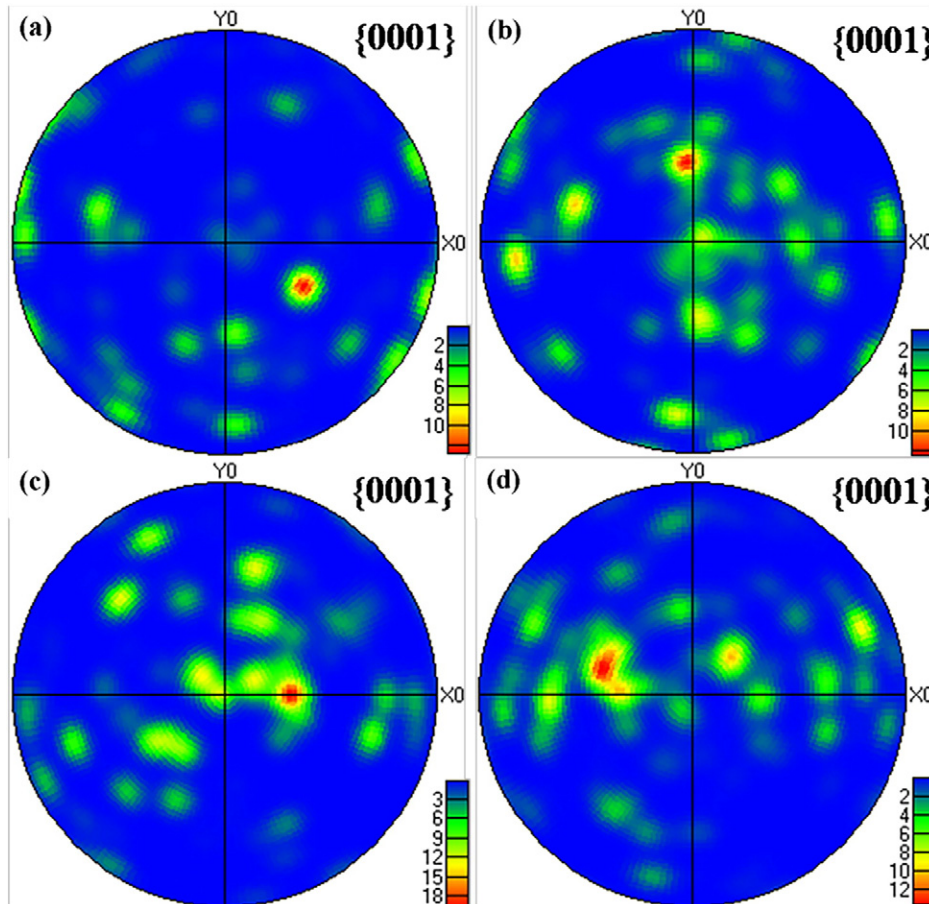


Fig. 2. $\{0001\}$ pole figures (PF) obtained from the top view for the SLM-processed Ti–45Al–2Cr–5Nb samples, (a) T_0 , (b) T_1 , (c) T_2 and (d) T_3 .

temperature at 523 K displays a significant influence on the crystallographic texture of the SLM-processed Ti–45Al–2Cr–5Nb alloy.

Fig. 3(a) illustrates the X-ray diffraction (XRD) results of the samples T_0 , T_1 , T_2 and T_3 from the top view. Apparently, only the diffraction peaks corresponding to α_2 , γ and B_2 phases are detected. It is worth noting that α and β are the high temperature disordered α_2 and B_2 , respectively. As revealed in the XRD patterns, the strong and dominant diffraction peak belonging to $(20\bar{2}1)\alpha_2$ is identified as the matrix phase. With increasing substrate preheating temperature, the intensities of the $(0002)\alpha_2$, $(20\bar{2}3)\alpha_2$ and $(20\bar{2}4)\alpha_2$ peaks decrease while the intensity of the $(20\bar{2}1)\alpha_2$ peaks increases. Meanwhile, the intensity of the $(202)\gamma$ peak increases whereas the $(620)\gamma$ and $(222)\gamma$ peaks basically remain unchanged. Similarly, the intensities of the $(220)B_2$ and $(311)B_2$ increase, whereas the $(420)B_2$ peak intensity decreases and $(310)B_2$, $(520)B_2$ peaks remain the same. Consequently, the α_2 phase decreases while the γ and B_2 phases increase with increasing substrate preheating temperature. According to previous literature [17–20], the phase transition of TiAl alloys during solidification has experienced a $L + \beta \rightarrow \alpha$ peritectic reaction, a $\alpha \rightarrow \beta + \gamma$ eutectic reaction and two $\alpha \rightarrow \alpha_2$, $\beta \rightarrow B_2$ ordering transformations. As the β is a high temperature stable phase, substrate preheating may improve the stability of the β phase. Moreover, due to the existence of strong β -stabilizer elements

of Cr and Nb [19], the stability of the β phase is further increased. But, the $L + \beta \rightarrow \alpha$ transformation will be restricted with the increase in the stability of the β phase. Meanwhile, the eutectic reaction rate of $\alpha \rightarrow \beta + \gamma$ is quite sensitive to the cooling rate [20], and substrate preheating can lower the cooling rate, thus facilitating the eutectic reaction. Therefore, the $L + \beta \rightarrow \alpha$ transformation is limited, while the $\alpha \rightarrow \beta + \gamma$ transformation is stimulated with increasing substrate preheating temperature, hence leading to the decrease of α_2 phase and the increase of γ and B_2 phases.

To further confirm the existence of α_2 , γ and B_2 phases in the SLM-processed Ti–45Al–2Cr–5Nb, TEM was conducted. In the bright-field image of T_3 in Fig. 3(b), fine grain γ and B_2 grains are found distributing in the α_2 matrix, and the fine B_2 grains are supposed to derive from the uncompleted transformation of primary $\beta \rightarrow \alpha$ [21]. Fig. 3(c) shows the selected area diffraction pattern (SADP) corresponding to Fig. 3(b). The different planes of the α_2 , γ and B_2 phases showing the diffraction rings can be identified, indicating the polycrystalline structures. The radius ratio of the rings observed from the SADP is 1:1.17 (D_{019}):1.44 (L_{10}):1.67 (bcc). Additionally, based on the standard XRD reference codes (12-0085, 65-0428 and 14-0451), the inter-planar spacings were calculated to be $d(10\bar{1}1) = 0.331$ nm (α_2), $d(11\bar{2}0) = 0.282$ nm (α_2), $d(111) = 0.230$ nm (γ), $d(200) = 0.198$ nm (B_2). Fig. 3(d) illustrates

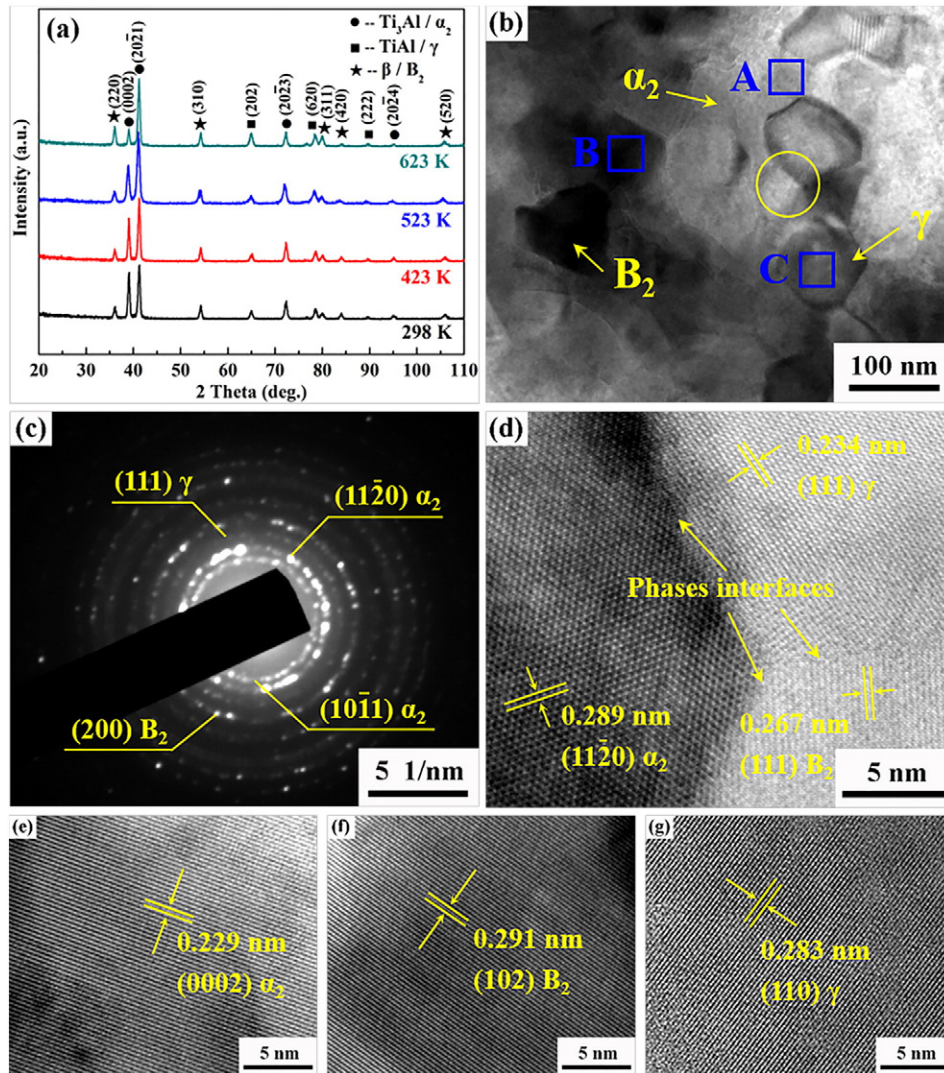


Fig. 3. (a) X-ray diffraction patterns of samples T_0 , T_1 , T_2 and T_3 ; (b) bright-field TEM images of T_3 sample; (c) selected area diffraction pattern (SADP) data obtained from Fig. 3(b); (d) HRTEM images of α_2 , γ and B_2 phase obtained from the yellow circled areas of Fig. 3(b); HRTEM images of single α_2 , γ and B_2 phase obtained from the zones A, B and C of Fig. 3(b) are presented in (e) (f) and (g), respectively.

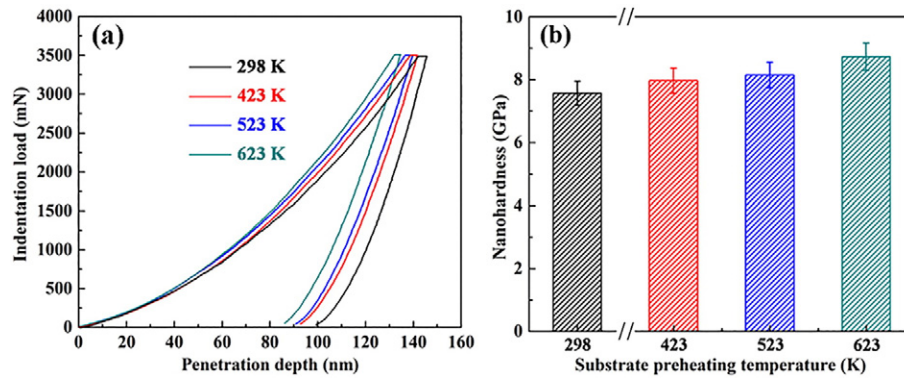


Fig. 4. (a) Loading-unloading curves and (b) calculated nanohardness values of the Ti-45Al-2Cr-5Nb processed by SLM at various substrate preheating temperatures.

the high resolution transmission electron microscopy (HRTEM) of α_2 , γ and B_2 phases in the yellow circle of Fig. 3(b). The lattice-fringe separations of 0.289 nm, 0.234 nm and 0.267 nm are identified as the (11 $\bar{2}$ 0) planes of α_2 (DO_{19}), the (111) planes of γ ($L1_0$) and (111) planes of B_2 (bcc), respectively. According to the measured lattice parameters and standard reference patterns, it can be concluded that the γ -related and B_2 -related phases simultaneously precipitate within the α_2 matrix. The γ and B_2 with the planes (11 $\bar{2}$ 0) α_2 //(111) γ //(111) B_2 in a range of several hundred nanometers are uniformly distributed within the α_2 matrix as shown in Fig. 3(b) [21,22].

In order to further study the single-phase features of α_2 , γ and B_2 , as well as their evolution mechanism, HRTEM was also conducted on the different zones of A, B and C in Fig. 3(b), and the corresponding HRTEM images are displayed in Fig. 3(e), (f) and (g), respectively. The lattice parameters were calculated to be $d(0002) = 0.229$ nm (α_2), $d(102) = 0.291$ nm (B_2) and $d(110) = 0.283$ nm (γ), which perfectly match the standard XRD PDF codes. As the (0002) α_2 and (110) γ phases are mainly derived from the (102) β phase [17,23], the phase evolution mechanism of the TiAl alloy in the SLM process can be concluded as follows: (102) β transforms to (0002) α_2 and (110) γ , and then the residual B_2 and incompletely transformed γ phase homogeneously distribute in the α_2 matrix.

Fig. 4(a) depicts the nanoindentation load-depth curves measured on the top sides of T_0 , T_1 , T_2 and T_3 . Obviously, the sample processed at room temperature (298 K) possesses the maximum indentation depth while the sample prepared at 623 K shows the smallest indentation depth. The indentation depth decreases gradually with increasing preheating temperature. As revealed in Fig. 4(b), the dynamic nanohardness H value of the sample processed without substrate preheating (7.57 ± 0.38 GPa at 298 K) is lower than those obtained at the preheating temperature of 423 K (7.96 ± 0.32 GPa), 523 K (8.14 ± 0.41 GPa) and 623 K (8.74 ± 0.42 GPa), and the nanohardness increases with the increase of the preheating temperature. In general, B_2 is the hardest phase among the B_2 , α_2 and γ phases ($B_2 > \alpha_2 > \gamma$) [7]. According to the XRD patterns shown in Fig. 3(a), the content of B_2 phase increases with increasing substrate preheating temperature. Therefore, the nanohardness tends to increase while the indentation depth gradually decreases when increasing substrate preheating temperature. Moreover, all the SLM-processed TiAl samples with or without the substrate preheating demonstrate superior nanohardness values compared to conventional casting processed TiAl alloy, which has a typical nanohardness of 4.8 ± 0.28 GPa [24]. Due to the distinctive layer-by-layer process of SLM, the residual stresses are usually large in SLM-fabricated samples, which may cause cracks [25]. But, residual stresses are not always detrimental. On the premise of a sufficiently high densification, the retention of a reasonable level of residual stress in SLM-processed parts favors the enhancement of hardness [26]. Moreover, the high cooling rate during SLM causes a very fine microstructure, which also gives rise to a further increase in the obtainable hardness.

Therefore, the SLM-processed TiAl shows much higher nanohardness than its traditional casting counterpart.

In summary, the grain orientations, crystallographic texture, phase composition and nanohardness can be tailored by controlling the substrate preheating temperature during SLM. With the optimal preheating temperature of 623 K, the basically equal existence of the grains with (0001), (10 $\bar{1}$ 1) and (11 $\bar{2}$ 1) orientations was successfully achieved. The phase evolution mechanism in the SLM-processed Ti-45Al-2Cr-5Nb alloy is concluded as follows: (102) β transforms to (0002) α_2 and (110) γ , and then the residual B_2 and incompletely transformed γ phase homogeneously distribute in the α_2 matrix. The orientation relationship between B_2 , α_2 and γ phases is expressed as (11 $\bar{2}$ 0) α_2 //(111) γ //(111) B_2 . Compared to the traditional casting TiAl alloy, the SLM-processed TiAl alloy shows much high nanohardness values ranging of 7.57 ± 0.38 GPa to 8.74 ± 0.42 GPa. The findings would be a valuable reference to the optimization of the substrate preheating temperature for fabricating TiAl components with acceptable grain structure and phase compositions and nanohardness by SLM.

This work was supported by the National Natural Science Foundation of China (51375189, 51375188) and National Defense Innovation Research Foundation Project of Huazhong University of Science and Technology. The authors would also like to thank the State Key Laboratory of Materials Processing and Die & Mould Technology as well as the Analysis and Testing Center of Huazhong University of Science and Technology for the EBSD and TEM tests.

References

- [1] L. Yu, X.P. Song, L. You, Z.H. Jiao, H.C. Yu, *Scr. Mater.* 109 (2015) 61–63.
- [2] X.H. Wu, A. Huang, D. Hu, M.H. Loretto, *Intermetallics* 17 (2009) 540–552.
- [3] Y.F. Wen, J. Sun, *Scr. Mater.* 68 (2013) 759–762.
- [4] K.N. Kulkarni, Y. Sun, A.K. Sachdev, E. Lavernia, *Scr. Mater.* 68 (2013) 841–844.
- [5] L.E. Murr, S.M. Gaytan, A. Ceylan, E. Martinez, J.L. Martinez, D.H. Hernandez, B.I. Machado, D.A. Ramirez, F. Medina, S. Collins, R.B. Wicker, *Acta Mater.* 58 (2010) 1887–1894.
- [6] X.H. Wu, *Intermetallics* 14 (2006) 1114–1122.
- [7] H.Z. Niu, Y.Y. Chen, S.L. Xiao, L.J. Xu, *Intermetallics* 31 (2012) 225–231.
- [8] Q.S. Wei, S. Li, C.J. Han, W. Li, L.Y. Cheng, L. Hao, Y.S. Shi, *J. Mater. Process. Technol.* 222 (2015) 444–453.
- [9] S. Zhang, Q.S. Wei, L.Y. Cheng, S. Li, Y.S. Shi, *Mater. Des.* 63 (2014) 185–193.
- [10] S.F. Wen, S. Li, Q.S. Wei, C.Z. Yan, S. Zhang, Y.S. Shi, *J. Mater. Process. Technol.* 214 (2014) 2660–2667.
- [11] L. Thijs, K. Kempen, J.P. Kruth, J.V. Humbeeck, *Acta Mater.* 61 (2013) 1809–1819.
- [12] L. Loeber, S. Biamino, U. Ackelid, S. Sabbadini, P. Epicoco, P. Fino, J. Eckert, *International Symposium, 22nd, Solid Freeform Fabrication*.
- [13] L. Löber, F.P. Schimansky, U. Kühn, F. Pyczak, J. Eckert, *J. Mater. Process. Technol.* 14 (2014) 1852–1860.
- [14] J. Gussone, Y.C. Hagedorn, H. Gherekhloo, G. Kasperovich, T. Merzouk, J. Hausmann, *Intermetallics* 66 (2015) 133–140.
- [15] C.Z. Yan, L. Hao, A. Hussein, P. Young, J.T. Huang, W. Zhu, *Mater. Sci. Eng. A* 628 (2015) 238–246.
- [16] U.F. Kocks, C.N. Tome, H.R. Wenk, *Texture and Anisotropy*, Cambridge University Press, Cambridge, 1998.
- [17] H. Clemens, H.F. Chladil, W. Wallgram, G.A. Zickler, R. Gerling, K.D. Liss, S. Kremmer, V. Güther, W. Smarsly, *Intermetallics* 16 (2008) 827–833.

- [18] G. Nie, H.S. Ding, R.R. Chen, J.J. Guo, H.Z. Fu, *Mater. Des.* 39 (2012) 350–357.
- [19] H.Z. Niu, Y.Y. Chen, Y.S. Zhang, J.W. Lu, W. Zhang, P.X. Zhang, *Intermetallics* 59 (2015) 87–94.
- [20] Y. Mishin, C. Herzig, *Acta Mater.* 48 (2000) 589–623.
- [21] M. Takeyama, S. Kobayashi, *Intermetallics* 13 (2005) 993–999.
- [22] L. Song, X.J. Xu, L. You, Y.F. Liang, Y.L. Wang, J.P. Lin, *Acta Mater.* 91 (2015) 330–339.
- [23] G. Yang, H.C. Kou, Y. Liu, J.R. Yang, J. Wang, S.Y. Zhang, J.S. Li, H.Z. Fu, *Intermetallics* 63 (2015) 1–6.
- [24] D.D. Zhu, D. Dong, C.Y. Ni, D.F. Zhang, Z.Z. Zhou, H.W. Wang, Z.J. Wei, *Mater. Charact.* 99 (2015) 243–247.
- [25] P. Mercelis, J.P. Kruth, *Rapid Prototyp. J.* 12/5 (2006) 254–265.
- [26] D.D. Gu, Y.C. Hagedorn, W. Meiners, G.B. Meng, R.J.S. Batista, K. Wissenbach, R. Poprawe, *Acta Mater.* 60 (2012) 3849–3860.